

# 3-D Basement Relief and Density Inversion Based on EfficientNetV2 Deep Learning Network

Yu Zhang<sup>1</sup>, Zhengwei Xu<sup>1</sup>, Minghao Xian<sup>1</sup>, Michael S. Zhdanov<sup>2</sup>, *Senior Member, IEEE*,  
Changjie Lai, Rui Wang<sup>1</sup>, Lifeng Mao<sup>1</sup>, and Guangdong Zhao<sup>1</sup>

**Abstract**—Gravity interface inversion is a critical technique in delineating the substructure of basins, providing essential technological and data support for oil and gas exploration. Traditional gravity inversion approaches often encounter issues such as suboptimal local solutions and limited resolution. Moreover, conventional deep learning inversion methods typically require extensive time for empirical parameter adjustment, hindering the achievement of optimal training outcomes. By utilizing Bouguer gravity anomaly data, this research pioneers the application of the EfficientNetV2 network in predicting 3-D basement relief interfaces and variations in overburden density. The network employs a composite scaling technique to adaptively adjust its width, depth, and input resolution, thereby identifying the most effective network configuration. Concurrently, the innovative Fused-MBconv convolutional module efficiently achieves superior results with a reduced number of network parameters. Specifically, in the Poyang Lake Basin study in Jiangxi Province, China, the EfficientNetV2 model demonstrated enhanced accuracy in predicting density variations of the basement interface and overlying strata compared to traditional methodologies.

**Index Terms**—Composite scaling technique, EfficientNetV2, fused-MBconv, gravity, inversion.

## I. INTRODUCTION

THE degree of basement relief in a sedimentary basin significantly influences the deposition of sediments and the formation of overlying structures. Tracing the boundaries of a concealed basement is crucial for understanding sedimentary structures and stratigraphy. Given the substantial density difference between sediment fill and the underlying basement,

the gravity method stands out as one of the most practical geophysical tools for delineating the basement framework. However, gravity inversion challenges in geophysics are typically categorized as ill-posed problems [1], [2], [3]. This ill-posed nature primarily arises from the disparity between the limited amount of observed data and the much larger number of model parameters that need to be resolved. Consequently, even minor variations in data can lead to significant impacts. Increasing the number of observation points does not always rectify the issue, as the kernel matrix may still exhibit linear correlations, failing to fully address the multiplicity of solutions and the instability inherent in the inversion problem. Given the variety of inversion methods available, selecting the most suitable one is crucial for effective exploration.

Conventional gravity inversion is typically categorized into deterministic inversion [4], [5], [6], [7], [8] and probabilistic inversion [9], [10], [11], [12], [13]. Common methods include the Newton iteration method [14], steepest descent method [15], and conjugate gradient method [16], [17], [18], [19]. These techniques utilize the gradient descent method to update model parameters, aiming to find the exact solution by constructing an objective function. However, such methods often reach local optima, failing to achieve global optima. In addition, due to the equal volume effect in gravity exploration, the accuracy of results can be compromised, often resulting in poor longitudinal resolution. To address these issues, regularization techniques and depth weighting functions have been employed [12], [13], [20], [21], [22], [23], [24], [25], [26]. Although these methods improve the stability and resolution of inversion results compared to smooth inversion, their reliance on special mathematical transformations limits their practical geological significance.

Probabilistic inversion methods, such as Monte Carlo methods [27], [28], [29], [30], adopt a stochastic approach to inversion, mitigating the tendency of gradient methods to converge on local minima. These methods, including random search [31], simulated annealing [32], and genetic algorithms [33], aim to generate prediction data that closely agree with observed data, targeting the global minimum of the error function. However, these methods often require a significant number of steps and optimization algorithms to improve the efficiency. Despite these advancements, challenges, such as the equal volume effect and the underdetermined nature of matrix operations in the gravitational field, persist.

In the context of basin analysis, the density of sedimentary layers within a basin is typically lower than that of

Manuscript received 20 March 2024; revised 8 June 2024; accepted 8 July 2024. Date of publication 16 July 2024; date of current version 30 July 2024. This work was supported in part by the Natural Science Foundation of Sichuan Province under Project 2024NSFSC0079 and Project 2023NSFSC0253, and in part by the National Natural Science Foundation of China under Project 42204090. (Corresponding author: Zhengwei Xu.)

Yu Zhang, Zhengwei Xu, Minghao Xian, Lifeng Mao, and Guangdong Zhao are with the Key Laboratory of Earth Exploration and Information Techniques, Ministry of Education, Chengdu University of Technology, Chengdu 610059, China (e-mail: yuzhang\_gem@163.com; zhengwei.xu@cdu.edu.cn; xmhcdut@163.com; mlf73@163.com; guangdongzhao@cdu.edu.cn).

Michael S. Zhdanov is with the Consortium for Electromagnetic Modeling and Inversion (CEMI), University of Utah, Salt Lake City, UT 84112 USA, and also with TechnoImaging, Salt Lake City, UT 84107 USA (e-mail: michael.s.zhdanov@gmail.com).

Changjie Lai is with the Engineering Geology Brigade of Jiangxi Bureau of Geology, Nanchang 330001, China, and also with Jiangxi Institute of Shale Gas Investigation and Development Research, Nanchang 330002, China (e-mail: laichangjie.0710@163.com).

Rui Wang is with the School of Computer Science and Technology, Changchun University of Science and Technology, Changchun 130022, China (e-mail: rwang@cust.edu.cn).

Digital Object Identifier 10.1109/TGRS.2024.3427711

the surrounding rocks, resulting in a distinct gravity low anomaly over the sedimentary basin. This anomaly can be instrumental in deducing the topographic characteristics of the basement [34], [35], [36], [37], [38], [39], [40]. Traditional methods, such as those proposed by Bott [41], Oldenburg [42], and Parker and Huestis [43], have provided foundational approaches for estimating basement depth and modeling density variations. However, these methods generally assume constant density and may not adequately address the variability in actual sedimentary environments.

The advancement of computer performance has significantly influenced the field of inversion problems, particularly through the integration of machine learning (ML) techniques. These methods involve injecting the obtained model into the inversion equation as a constraint, which effectively reduces the issue of multiple solutions in inversion problems. In gravity inversion, unsupervised learning methods predict geological body models using functions, such as clustering [44], linear classifiers [45], support vector machines [46], decision trees [47], and regression algorithms [48], [49], [50]. However, unsupervised methods have limitations in adequately assessing the association between the model and the data, posing challenges in fully realizing the potential of ML in enhancing the accuracy and reliability of gravity inversion outcomes.

In the domain of supervised learning, extensive datasets are constructed to address regression and classification issues, establishing implicit relationships between data. Deep learning, particularly convolutional neural networks (CNNs), has gained prominence in gravity inversion due to advantages such as local connections, weight sharing, enhanced generalization capabilities, and transfer learning abilities [51], [52], [53]. However, traditional CNN structures primarily extract shallow features, leading to issues such as inadequate global information representation.

To address these challenges, researchers have developed advancements such as ResU-Net++ [54], which mitigates the loss of global information during feature extraction by concentrating on the last one or two layers of the training process and incorporating U-Net [55], [56], [57] structures for upsampling and downsampling. However, ResU-Net++ has limitations, such as prediction accuracy plateauing beyond a certain point of learning.

The EfficientNetV1 network [58] introduces a compound scaling strategy that adaptively determines the depth, width, and optimal structural parameters for input data resolution. This approach circumvents the limitations of network performance resulting from empirical operations. EfficientNetV2 [59] further enhances this by using the Fused-MBConv convolution module to minimize redundant convolution operations, ensuring efficient feature extraction from complex data with fewer training parameters. Despite these advancements, EfficientNetV2 is predominantly used for image classification, with limited application in geophysical inversion regression prediction.

In this article, we deploy the EfficientNetV2 network to predict the undulating interface of a 3-D basement and the density variations of the overlying strata. The main three key contributions in our approach involve: 1) recovering both undulating

interface and the overlapping density variation simultaneously; 2) the Gaussian filtering method is employed to smooth the disturbance interface, combined with the acquired Bouguer gravity anomaly data, to rapidly construct an actual training dataset; and 3) in the stage of synthetic study, we compare the prediction results of EfficientNetV2 with those obtained from CNNs and ResU-Net++ network structures. In real cases, the well-trained EfficientNetV2 network is used to predict both the three-layer undulating interface and the density changes of the overlying stratum in the Poyang Lake Basin. To validate the accuracy of our prediction results, we compare them with the outcomes of traditional smooth inversion methods, reinforced by existing seismic and logging data, providing a comprehensive assessment of the EfficientNetV2 network's predictive capabilities in geophysical applications.

## II. INVERSION METHOD BASED ON EFFICIENTNETV2 NETWORK

Conventional 3-D basin basement inversion using gradient optimization algorithms can estimate the magnitude of the overlying anomaly density and naturally depict the geometric shape of the basin basement, leveraging the distinct difference between overlying density and surrounding rock density. In this article, we employ supervised deep learning to predict both the density variation and the basin basement relief simultaneously. It is worth emphasizing that, within the framework of deep learning, these two properties (as labels) are predicted separately.

Employing a supervised deep learning approach, constructing a comprehensive training dataset for both input and output is essential. The data processing workflow is illustrated in Fig. 1. During the training dataset phase, we start by establishing the basement depth ( $Z$ ) and the density change factor ( $\beta$ ) as the output labels. These labels are derived based on the measured gravity data of the target area. Subsequently, the Bouguer gravity field ( $g_{\text{iso}}$ ), generated from the basin model integrated with these labels, serves as the input data for the deep neural network. Building upon this foundation, we train the EfficientNetV2 network by fine-tuning the hyperparameters. This process involves constructing and determining the parameters of the EfficientNetV2 network. Following this, we use the network to predict real gravity data. This prediction enables us to accurately delineate the 3-D basement relief and the corresponding density changes in the overlying strata. The culmination of this process is the development of a high-precision geological model of the basement. This model not only reflects the complexities of the basin's structure but also provides valuable insights for further geological exploration and analysis.

### A. Generation of Training Sets

1) *Construct Basement Depth (Simulation Verification)*: To validate the efficacy of the EfficientNetV2 network structure in predicting geological models of basins, we constructed a dataset for the basement depth ( $Z$ ) specifically for simulation verification [51]. The initial step involved obtaining the initial basement interface ( $Z_{\text{Initial}}$ ) through the Bouguer plate model,

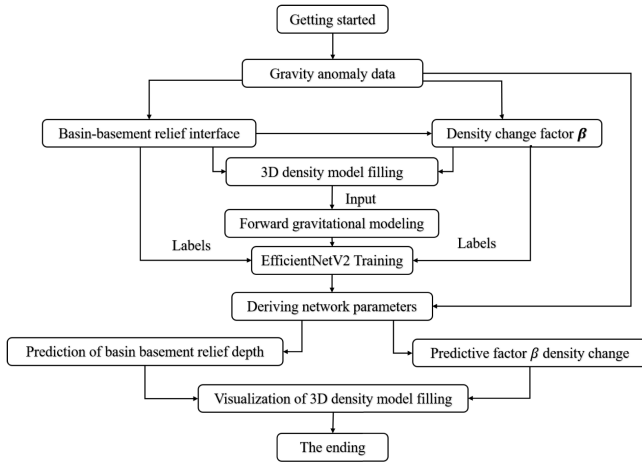


Fig. 1. Workflow of gravity inversion based on EfficientNetV2.

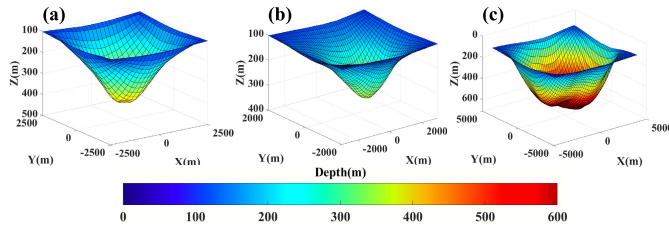


Fig. 2. Three different base depth models. (a) Symmetric model. (b) Asymmetric model. (c) Complex model.

as delineated in (1), utilizing measured Bouguer gravity data. Subsequently, we employed the random midpoint displacement method to generate a total of 74 640 sets of sedimentary basin disturbance interface datasets. This was followed by the application of the Hadamard operation to amalgamate these disturbance interface datasets with  $Z_{\text{Initial}}$ . As a result, we produced 74 640 sets of basement relief model datasets, denoted as  $\{Z_{\text{SMU}}^{\psi}\}_{\psi=1}^{N_{\text{SMU}}}$ ,  $N_{\text{SMU}} = 74\,640$

$$Z_{\text{Initial}} = \frac{g_{\text{iso}} \Delta \rho_0}{41.89 \Delta \rho_0^2 + \alpha g_{\text{iso}}} \quad (1)$$

where  $g_{\text{iso}}$  symbolizes the Bouguer gravity anomaly,  $\Delta \rho_0$  indicates the difference between ground density and basement density, and  $\alpha$  represents the gradient of density with depth. This comprehensive approach ensures a robust framework for assessing the predictive power of the EfficientNetV2 network in geological modeling of basins.

These datasets were further categorized into three distinct types based on basement relief patterns: symmetric models, asymmetric models, and complex models, as depicted in Fig. 2. In alignment with the standard practice in the geophysical field, where the ratio of observation length to model depth should be within the range of  $10 \leq W/H \leq 15$ , the relief depth of the basement in all datasets is approximately between 300 and 800 m. The lateral extent of the basin model varies from 3000 to 8000 m.

2) *Construct Basin Basement Depth (Actual Data)*: When applying deep learning to process real-world data, it is crucial to recognize that different work areas may require distinct basement relief models as training datasets. Relying solely on

a unified training dataset can lead to limitations, as such a dataset may not fully encapsulate the specific geological conditions of the actual work area. Consequently, this could result in predictions that do not accurately reflect real geological conditions. To enhance the accuracy of basin inversion, it is imperative to construct and utilize a dataset that aligns with the geological characteristics of the basement in the targeted work area. This approach necessitates retraining the parameters to fit the structure of the deep learning network more appropriately.

In this study, we initially determine the initial basement relief interface through conventional gravity smoothing inversion, as illustrated in Fig. 3(a). To generate the disturbance interface, we employ a random noise generation method with a mean value of 0 and a standard deviation ranging from 0% to 70% of the maximum depth of the initial interface. This method is used to construct 3000 sets of noise fluctuation interfaces, as depicted in Fig. 3(b). Given that the basement interface of sedimentary basins tends to be smooth due to stratum pressure, we apply a 2-D Gaussian smoothing filter (with a standard deviation of 3) to all noise disturbance interface data. In this process, the  $H_{\text{dis}}$  matrix of noise interface fluctuation data is of size  $(2k + 1) \times (2k + 1)$ . The filtered noise interface data,  $H_{\text{dis}}(i, j)$ , is then detailed in (2), ensuring a more realistic representation of the geological features for effective deep learning application

$$H_{\text{dis}}(i, j) = \frac{1}{2\pi\sigma^2} \exp\left(-\frac{(i-k-1)^2 + (j-k-1)^2}{2\sigma^2}\right) \quad (2)$$

where  $\sigma$  represents the standard deviation and  $(i, j)$  represents the positions of matrix elements. After undergoing Gaussian filtering, the noise disturbance interface acquires a smoothly undulating shape, as clearly depicted in Fig. 3(c). This process results in a more realistic and geologically plausible interface representation. Subsequently, we combine the initial basement interface fluctuations with the smoothed disturbance interface. This step culminates in the creation of 3000 distinct sets of basement interface fluctuation data  $\{Z_{\text{ATU}}^{\psi}\}_{\psi=1}^{N_{\text{ATU}}}$ ,  $N_{\text{ATU}} = 3000$ , as shown in Fig. 3(d). Each set in this comprehensive dataset effectively captures the nuanced variations and characteristics of the basement interface, providing a robust foundation for further analysis and modeling in our study.

3) *Dataset Density Padding*: The Bouguer gravity anomaly is primarily attributed to variations in density, thus necessitating the inclusion of density characteristics in the construction of basement interface fluctuation models. In sedimentary basins, due to the influence of formation pressure, the density of the sedimentary layer tends to converge with the density of the surrounding basement rock as depth increases. However, He et al. [51] focused solely on predicting the relief depth of the basement interface using a CNN network, without addressing the changes in the density of the overlying strata of the basin.

To bridge this gap, our study introduces a hyperbolic variable density function, incorporating the density change factor  $\beta$ . This function is utilized to accurately fill in the calculations for the sedimentary basin model, as detailed in Sections II-A1 and II-A2. The variation of density  $\Delta \rho(z)$  with depth is represented in (3) [60]. From the formula, it can be found

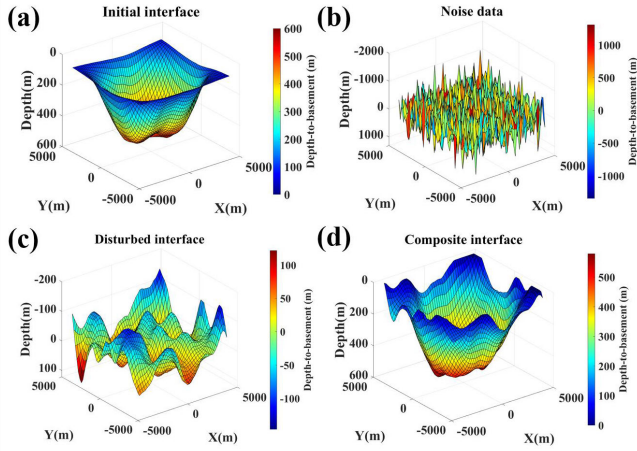


Fig. 3. Schematic diagram of the initial interface disturbance. (a) Initial interface of the inversion result. (b) Standard deviation ranging from 0% to 70% of the maximum depth of the initial interface. (c) Smooth disturbance interface by 2-D Gaussian filtering of random noise. (d) Final interface by superposition the initial interface and the perturbation interface.

that the resulting density is continuous. This approach ensures a more comprehensive and realistic modeling of the basin basement, accounting for both the topographical variations and the critical aspect of density changes within the sedimentary layers

$$\Delta\rho(z_{i,j,k}) = \frac{\Delta\rho_0\beta_{i,j}}{(\beta_{i,j} + z_{i,j,k})^2}, \quad i = 1, 2, \dots, N_x$$

$$j = 1, 2, \dots, N_y; \quad k = 1, 2, \dots, N \quad (3)$$

where  $\Delta\rho_0$  represents the difference between the density of the top interface and the density of the surrounding rock. For the above three models, we use uniform and identically sized  $\Delta\rho_0$  matrix, and  $z_{i,j,k}$  represents the depth of the sedimentary basin shown in (4).  $N_x$  and  $N_y$  are the number of grids divided along the  $x$ - and  $y$ -directions, respectively, in the underground inversion space, and  $N$  is the number of rectangular units divided into equal intervals for each prism.  $\beta_{i,j}$  stands for the factor controlling the density of sedimentary basins in the  $i, j$  prism with depth variation, and its expression is shown in the following equation:

$$z_{i,j,k} = \frac{N-1}{N}H_{i,j}, \quad i = 1, 2, \dots, N_x$$

$$j = 1, 2, \dots, N_y; \quad k = 1, 2, \dots, N \quad (4)$$

$$\beta_{i,j} = \frac{\widetilde{\Delta\rho}_{i,j}H_{i,j}}{(\Delta\rho_0 - \widetilde{\Delta\rho}_{i,j})}$$

$$i = 1, 2, \dots, N_x; \quad j = 1, 2, \dots, N_y \quad (5)$$

where  $\widetilde{\Delta\rho}_{i,j}$  represents the weighted average density (equivalent density) of the  $i, j$  prism and  $H_{i,j}$  represents the maximum depth of the  $i, j$  prism in the sedimentary basin. It is obvious that  $\beta_{i,j}$  is jointly determined by  $\Delta\rho_0$  and the weighted average density  $\widetilde{\Delta\rho}_{i,j}$  of the whole set of strata. For each actual working area, the weighted average density ( $\widetilde{\Delta\rho}_{i,j}$ ) of the sedimentary basin is determined by the geological conditions

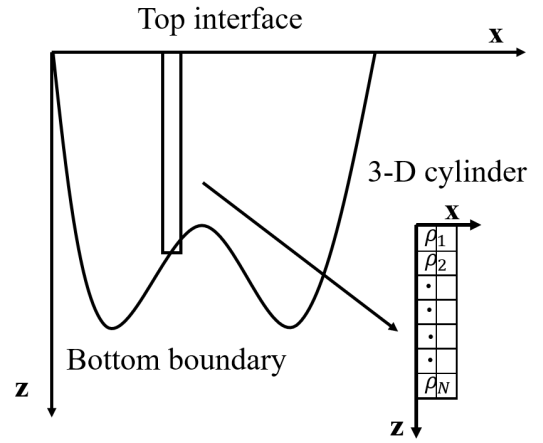


Fig. 4. Rectangular grid cell division, showing the graph along the  $X$ - $Z$  section.

of the area. However, using the average density  $\Delta\rho_0$  to construct a model controlled by density change factors may have limitations, especially in areas with significant basement fluctuations. In contrast, the basement fluctuation of the Poyang Lake Basin is relatively gentle, and the strata are continuous. Therefore, calculating the weighted average density ( $\widetilde{\Delta\rho}_{i,j}$ ) requires relying on the real Bouguer gravity anomaly data of the sedimentary basin ( $g_{iso}$ ) and the basement depth ( $H_{i,j}$ ) of the sedimentary basin as shown in the following equation [60]:

$$\widetilde{\Delta\rho}_{i,j} = \frac{g_{iso}}{2\pi GH_{i,j}}, \quad i = 1, 2, \dots, N_x; \quad j = 1, 2, \dots, N_y \quad (6)$$

where  $G$  is the universal gravitational constant ( $G = 6.67384 \times 10^{-11} \text{m}^3 \cdot \text{kg}^{-1} \cdot \text{s}^2$ ).

4) *Gravity Forward Modeling*: In the process of inversion research using supervised learning, an essential step involves computing the gravity anomaly data,  $\Delta g_z$ , which serves as the input for the deep neural network. The crucial precondition for obtaining this gravity anomaly data is the construction of a basin density model. To this end, the density variation factor,  $\beta_{i,j}$ , for the 3-D basin is employed to calculate the density of each equally spaced rectangular element within the  $i$ th and  $j$ th prisms. This calculation follows the guidelines set out in (3) and the resulting densities ( $\Delta\rho_{i,j,1}, \Delta\rho_{i,j,2}, \dots, \Delta\rho_{i,j,N}$ ) are then filled in accordingly, as illustrated in Fig. 4. Upon establishing the basin density model, we then acquire the necessary gravity anomaly data for two key stages: the simulation verification stage and the actual data processing stage. For the former, we obtain a dataset of  $\{\Delta g_{SMU}^{\psi}\}_{\psi=1}^{N_{SMU}}$ ,  $N_{SMU} = 74\,640$ , and for the latter, we gather a dataset of  $\{\Delta g_{ATU}^{\psi}\}_{\psi=1}^{N_{ATU}}$ ,  $N_{ATU} = 3000$ . These datasets are crucial for evaluating the effectiveness of the inversion process and ensuring the accuracy of the deep learning model in real-world applications.

The calculation formula of  $\Delta g_z$  of gravity anomaly data is shown in the following equation:

$$\Delta g_z(x, y, z) = -G \iiint_V \frac{\Delta\rho(\xi, \eta, \zeta)(z - \zeta)}{R^3} d\xi d\eta d\zeta$$

$$R = \sqrt{(x - \xi)^2 + (y - \eta)^2 + (z - \zeta)^2} \quad (7)$$

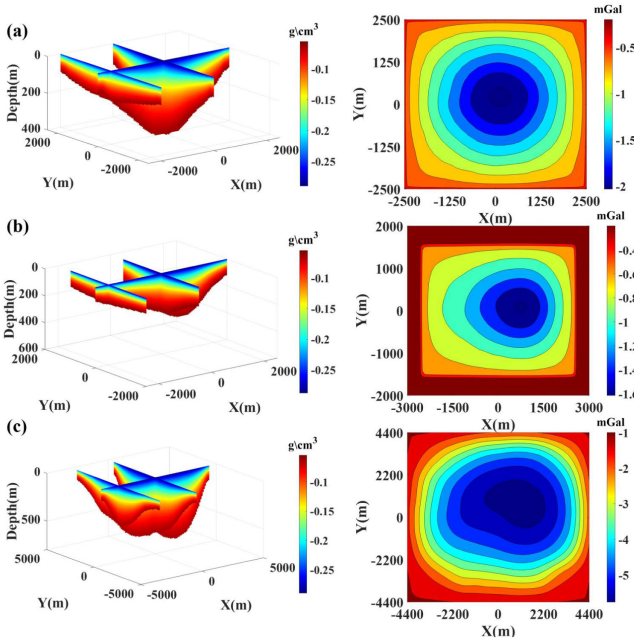


Fig. 5. Spatial density filling and forward field diagrams are presented for three distinct models. The first column represents the dataset label outputs  $\{Z_{SMU}^{\psi}, \beta_{SMU}^{\psi}\}$ , detailing the basement depth and the associated density change factor. The second column, on the other hand, displays the Bouguer gravity anomalies  $\{\Delta g_{SMU}^{\psi}\}$  at the dataset outputs. (a) Vertical slice diagram of the symmetric model. (b) Vertical slice diagram of the asymmetric mode. (c) Vertical slice diagram of the complex model, showcasing its intricate and multifaceted nature.

where  $(\xi, \eta, \zeta)$  represents the coordinates of the center point of the underground subdivision grid,  $(x, y, z)$  represents the coordinates of the ground observation point,  $\Delta\rho$  represents the density, and  $R$  represents the data of the observation point and the coordinates of the center point.

We have now successfully compiled all the datasets necessary for the deep neural network. This comprehensive collection includes the dataset labels  $\{Z_{SMU}^{\psi}, \beta_{SMU}^{\psi}\}_{\psi=1}^{N_{SMU}}$ ,  $N_{SMU} = 74\,640$ , and the corresponding input datasets  $\{\Delta g_{SMU}^{\psi}\}_{\psi=1}^{N_{SMU}}$ ,  $N_{SMU} = 74\,640$ , for the packet simulation verification stage. These are depicted in Fig. 5. Similarly, for the actual data processing stage, we have prepared the dataset labels  $\{Z_{ATU}^{\psi}, \beta_{ATU}^{\psi}\}_{\psi=1}^{N_{ATU}}$ ,  $N_{ATU} = 3000$ , and the input datasets  $\{\Delta g_{ATU}^{\psi}\}_{\psi=1}^{N_{ATU}}$ ,  $N_{ATU} = 3000$ . In these datasets,  $\beta_{SMU}$  and  $\beta_{ATU}$  denote the density change factors of the basin basal interface fluctuation dataset for the simulation verification stage and the actual data processing stage, respectively. To optimize the training of the deep neural network, we strategically allocate 80% of the dataset for training purposes and reserve the remaining 20% for validation. This division ensures a balanced approach, allowing for thorough training of the network while also providing sufficient data to effectively evaluate its performance and accuracy.

### B. EfficientNetV2 Network Structure

This study aims to reconstruct the fluctuating form of the 3-D basement interface and the density changes in the overlying strata from 2-D gravity data. To achieve this, we uti-

TABLE I  
EFFICIENTNETV2-S NETWORK STRUCTURE TABLE

Stage	Operator	Stride	#Channels	#Layers
0	Conv3x3	2	24	1
1	Fused-MBConv1, k3x3	1	24	2
2	Fused-MBConv4, k3x3	2	48	4
3	Fused-MBConv4, k3x3	2	64	4
4	MBConv4, k3x3, SEO.25	2	128	6
5	MBConv4, k3x3, SEO.25	1	160	9
6	MBConv4, k3x3, SEO.25	2	256	15
7	Conv1x1 & Pooling & FC		1280	1

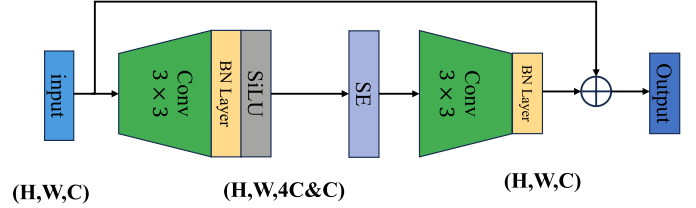


Fig. 6. Convolutional structure of Fused-MBconv, where BN layer is batch normalization and SiLU is the activation function.

lize the EfficientNetV2-S deep learning network structure based on multichannel and lightweight convolution technology. This network is specifically designed to potentially map the relationship between Bouguer gravity anomaly data and the sedimentary basin model. The architecture of the network is detailed in Table I.

Upon examination of the network structure, it is evident that it comprises seven stages. This design deviates from traditional CNNs in several ways. In stages 0 and 7, the network employs common convolutional kernels, each followed by a pooling layer and activation function, and concludes with either a fully connected layer or a pooling layer. The distinct feature of this network, however, lies in the incorporation of two innovative convolution modules: Fused-MBconv and MBconv. These modules are pivotal in enhancing the network's efficiency and accuracy in mapping the complex geological features from the gravity data, thereby offering a more nuanced understanding of the basin's subsurface characteristics.

#### 1) Convolutional Module Structure of Fused-MBconv:

In the original EfficientNetV1 deep learning network, the MBconv convolution module is predominantly used in all stages, except for the conventional convolution in the first and last steps, as outlined in Table I. While the MBconv convolution module can extract feature matrices using fewer parameters than traditional convolution operations, its extensive use of convolutions does not significantly enhance the training speed. To address this issue, the EfficientNetV2-S network employs the Fused-MBconv convolution module, which reduces the number of operations by amalgamating multiple convolutions found in the traditional MBconv. This adaptation maintains the effectiveness of convolution while decreasing the convolution operation layers, especially for large-size inputs. However, it is important to note that the MBconv convolutional structure may be better suited for processing detailed and complex features, so it should not be replaced with Fused-MBconv solely for speed improvement. The structure of this module is illustrated in Fig. 6.

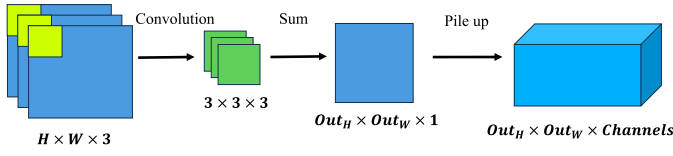


Fig. 7. Traditional  $3 \times 3$  convolution kernel for ascending feature extraction operation.

The Fused-MBConv convolution module first utilizes a  $3 \times 3$  standard convolution kernel on the main branch to transform the low channel input feature matrix into multichannel data (high-dimensional feature vectors), thereby gaining more receptive fields through ascending dimension processing, as depicted in Fig. 7. For instance, if the input feature matrix size is  $H \times W \times 3$  (where 3 represents the number of channels), the convolution kernel parameter required is  $FMB^{para} = 3 \times 3 \times 3 \times \text{channels} = 27$  channels. If the number of channels increases to 5,  $FMB^{para} = 3 \times 3 \times 5 \times \text{channels} = 45$  channels.

Subsequently, the high-dimensional feature matrix undergoes nonlinear transformation via the batch normal layer and the activation function layer (SiLU). The squeeze-and-excitation (SE) module then processes this matrix, extracting key features and suppressing noise data to enhance the network's representation capability (detailed in Section II-B2.a). A new feature matrix is obtained through dimensionality reduction using a traditional  $1 \times 1$  convolution kernel. This matrix is then combined with the input feature matrix through a shortcut connection, requiring the dimensions of both matrices to match. This shortcut connection significantly improves gradient propagation across multiple layers, facilitating efficient training of networks with extensive layers. The expansion ratio in the Fused-MBconv convolution module, either 1 or 4 as shown in stages 1–3 in Table I, is crucial. It determines the number of channels the ascending convolution operation is raised to, essentially dictating the extent of channel increase during the first convolution operation.

2) *MBconv Convolution Module Structure*: Similar to the Fused-MBconv module discussed in Section II-B1, this module initially converts the low channel input feature matrix into a high-dimensional feature matrix, thereby expanding the receptive fields through dimension increase. Subsequently, the high-dimensional feature matrix undergoes nonlinear transformation via the batch normal layer and the activation function layer (SiLU). However, a notable difference from the Fused-MBconv is the use of a  $1 \times 1$  convolution kernel instead of a  $3 \times 3$  kernel. This is followed by a  $3 \times 3$  depth-separable convolution (DWconv) to enhance the convolutional receptive field and extract features (detailed in Section II-B2.b). The features obtained are then processed by the SE module, which adjusts the feature matrix.

The final step involves obtaining a new feature matrix through dimensionality reduction using a traditional  $1 \times 1$  convolution kernel. This new feature matrix is then combined with the original input feature matrix through a shortcut connection. This shortcut requires that the dimensions of the input feature matrix and the new feature matrix match. This approach,

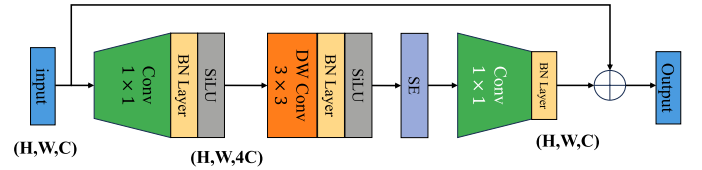


Fig. 8. MBconv convolution structure and its internal convolution layer.

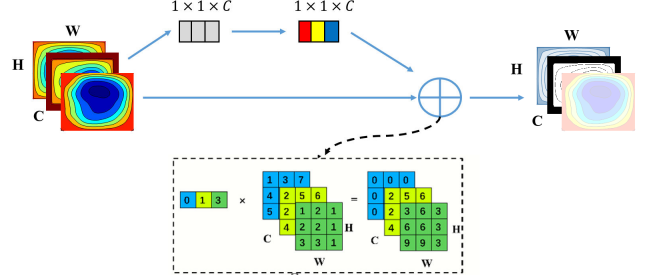


Fig. 9. SE module and Bouguer gravity anomaly feature extraction.

as illustrated in Fig. 8, ensures efficient integration of the newly extracted features with the original data, enhancing the overall efficacy and accuracy of the feature processing in the neural network.

a) *SE module structure*: The SE module plays a pivotal role in intelligently recalibrating channel characteristics during the processing of gravity data. It adeptly emphasizes key features by assigning greater weights to more informative channels while simultaneously reducing noise and less relevant elements by attenuating their corresponding channels. This selective emphasis and suppression streamline the network's operation, significantly enhancing its capability to discern complex patterns within gravity data, a critical aspect of geophysical analysis.

In the S-E operation, the input matrix  $U \in R^{H \times W \times C}$  is condensed into a vector  $F_{sq}(u_c)$  via global pooling, as indicated in the following equation:

$$F_{sq}(u_c) = \frac{1}{H \times W} \sum_{i=1}^H \sum_{j=1}^W u_c(i, j) \quad (8)$$

where  $u_c(i, j)$  denotes the  $c$ th element in the input matrix  $U \in R^{H \times W \times C}$ . The terms  $H$  and  $W$  represent the number of rows and columns, respectively, in the overall designed number of channels ( $C$ ), from which gravity input data are extracted through the convolution operation. The application of the specific S-E module in identifying gravity anomaly data is illustrated in Fig. 9, where the process involves multiplying the matrix derived from each figure's data to yield the final result. The S-E block is adept at learning channel correlations, thereby enhancing the network's sensitivity to crucial channels. Concurrently, it suppresses redundant or irrelevant features that could otherwise act as noise, potentially impeding the effectiveness of the prediction. This intricate process of modulation and enhancement within the S-E module is integral to the network's ability to accurately interpret and analyze gravity anomaly data.

b) *DWconv modular architecture*: The DWconv module and the traditional convolution module in the MBconv

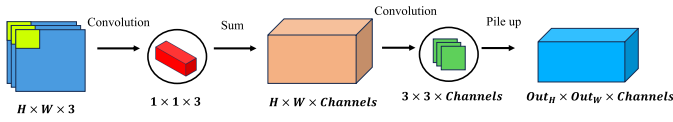


Fig. 10. MBconv convolution structure. (a) Calculation method of the  $1 \times 1$  convolution kernel. (b) DWconv kernel.

module both engage in feature extraction from the upper level matrix. However, a key distinction of the DWconv module is that it does not perform a summation operation across channels after convolution, as depicted in Fig. 10(b). This means that the number of channels in the DWconv module's convolution kernel must match the number of channels in the upper level matrix. Unlike traditional convolution, where post-convolution, all channels are summed up, the DWconv module skips this step.

With the implementation of the DWconv module, the convolution kernel parameter  $MB^{\text{para}}$  for the same feature matrix size as shown in Fig. 7 is calculated to be  $1 \times 1 \times 3 \times \text{channels} + 3 \times 3 \times \text{channels} = 12$  channels. In contrast, the convolution kernel parameters required by the Fused-MBconv module depend on both the number of matrix channels in the upper level and the size of the convolution kernel. Meanwhile, for the MBconv module, the convolution kernel parameters are influenced solely by the number of matrix channels in the upper level.

Consequently, the DWconv module offers a speed advantage in training lightweight networks. By forgoing the channel summation step and requiring fewer parameters for the same feature extraction, the DWconv module streamlines the convolution process. This efficiency makes it particularly well-suited for applications where training speed and resource optimization are crucial.

3) *Composite Scaling Technique*: In many CNNs, researchers typically employ a fixed variable method for training network models. This method involves selecting one parameter from the network's depth, width, or the resolution of the input image and then fixing the other two parameters based on experience. However, this approach requires extensive manual tuning and does not guarantee an optimal combination of these three parameters. To address this challenge, EfficientNetV2 utilizes a compound scaling technique.

This technique begins by defining the entire EfficientNetV2 network as a variable, Net, whose formula is given as follows:

$$\text{Net}(d, w, r) = \bigodot_{i=1, \dots, s} N_s(X_{1 < H_1, W_1, r >}) \quad (9)$$

where Net consists of  $s$  stages, and  $d$ ,  $w$ , and  $r$  denote the depth, width, and resolution of the EfficientNetV2 network, respectively.  $X_1$  represents the input data in the deep neural network, with  $< H_1, W_1, r >$  defining the height, width, and the number of channels of  $X_1$ , respectively. The output tensor of  $N_s$  after  $s$  stage is expressed as follows:

$$N_s = F_s^k \odot \dots \odot F_s^1(X_s^i) = \bigodot_{(i=1, \dots, k)} F_s^i(X_s^i). \quad (10)$$

The convolution operation at layer  $i$  in stage  $s$  from Table I is defined as  $F_s^i$ . The input feature tensor at layer  $i$  in stage  $s$  is  $X_s^i$ , and the output feature tensor  $Y_s^i$  for the same layer is calculated in the following equation:

$$Y_s^i = F_s^i(X_s^i). \quad (11)$$

To find the best structure, the depth ( $d$ ), width ( $w$ ), and resolution ( $r$ ) of all layers in the EfficientNetV2 network are scaled by a constant proportion. The goal is to maximize the model's accuracy within the constraints of available resources by the following equation:

$$\begin{aligned} & \max_{d, w, r} \text{Accuracy}(\text{Net}(d, w, r)) \\ & \text{s.t. } N(d, w, r) = \bigodot_{i=1, \dots, s} \widehat{F}_s^{d \cdot \widehat{r}_i} (X_{< r, \widehat{H}_i, r, \widehat{W}_i, w, \widehat{C}_i >}) \\ & \text{Memory}(\text{Net}) \leq \text{targetmemory} \\ & \text{FLOPS}(\text{Net}) \leq \text{targetflops} \end{aligned} \quad (12)$$

where the predefined parameters  $\widehat{F}_i$ ,  $\widehat{L}_i$ ,  $\widehat{H}_i$ ,  $\widehat{W}_i$ , and  $\widehat{C}_i$  are adjusted based on the resolution of the input image. If the input image is high resolution, the network's receptive field should be increased to capture more features. The composite coefficient  $\phi$  is defined to uniformly scale the depth ( $d$ ), width ( $w$ ), and resolution ( $r$ ) of the network by the following equation:

$$\begin{aligned} & \text{depth: } d = \alpha^\phi \\ & \text{width: } w = \beta^\phi \\ & \text{resolution: } r = \gamma^\phi \\ & \text{s.t. } \alpha \cdot \beta^2 \cdot \gamma^2 \approx 2, \alpha \geq 1, \beta \geq 1, \gamma \geq 1. \end{aligned} \quad (13)$$

Ultimately, we selected the EfficientNetV2-S architecture (as outlined in Table I) as our baseline training framework. This model features a width magnification factor of 1.4 and a depth magnification factor of 1.8, balancing the network's dimensions for optimized training and performance.

4) *Termination of the Training*: To assess the stability of various EfficientNetV2-based networks, this study utilizes the normalized misfit as a metric to quantify the gravity observation loss during training. The normalized misfit is calculated using the following formula:

$$\begin{aligned} Z_{\text{misfit}} &= \frac{\|Z_{\text{pre}} - Z_{\text{True}}\|^2}{\|Z_{\text{True}}\|^2} \\ \beta_{\text{misfit}} &= \frac{\|\beta_{\text{pre}} - \beta_{\text{True}}\|^2}{\|\beta_{\text{True}}\|^2} \end{aligned} \quad (14)$$

where  $\|\cdot\|$  stands for norm operator,  $Z_{\text{True}}$  denotes the actual depth of the basement relief interface, and  $Z_{\text{pre}}$  represents the predicted depth of the basement relief interface. Consequently,  $Z_{\text{misfit}}$  stands for the normalized error in the depth prediction of the basement undulating interface. Similarly,  $\beta_{\text{True}}$  denotes the true density change factor,  $\beta_{\text{pre}}$  refers to the predicted density change factor, and  $\beta_{\text{misfit}}$  signifies the normalized error in the predicted density change factor.

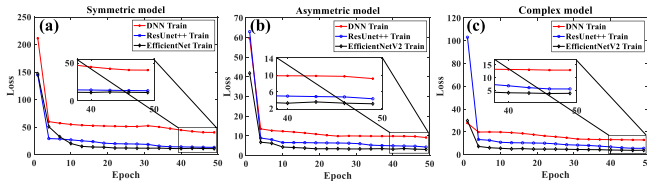


Fig. 11. Loss function comparison for three different networks trained on three different models. (a) Symmetric model loss function curve. (b) Loss function curve of asymmetric model. (c) Loss function curve of complex model.

TABLE II

COMPARISON OF LEARNING PARAMETERS FOR THE THREE NETWORKS

Network Parameters	Symmetric model	Asymmetric model	Complex model
DNN	42.8Mb	80.78Mb	80.398Mb
ResUnet++	365Mb	180Mb	376Mb
EfficientNetV2	86.4Mb	95Mb	99.962Mb

### III. SYNTHETIC STUDIES

#### A. Network Training

To optimize the training of the EfficientNetV2 network model, we utilize the dataset from the simulation verification stage (Section II-A1) as our training dataset. Specifically,  $\{\Delta g_{SMU}^{\psi}\}_{\psi=1}^{N_{SMU}}$ ,  $N_{SMU} = 74\,640$ , serves as the input dataset for the deep neural network. The corresponding output label dataset is  $\{Z_{SMU}^{\psi}, \beta_{SMU}^{\psi}\}_{\psi=1}^{N_{SMU}}$ ,  $N_{SMU} = 74\,640$ . We allocate 80% of this dataset for training and reserve the remaining 20% for validation.

Fig. 11 presents a comparative analysis of the loss functions across three types of basin density models, using three different deep learning networks. In this figure, the red line indicates the loss function curve of the DNN network model, the blue line represents the loss function curve of the ResU-Net++ network model, and the black line corresponds to the loss curve of the EfficientNetV2 network. Fig. 11(a) shows the training loss function comparison for the symmetric model, Fig. 11(b) shows the training loss function comparison for the asymmetric model, and Fig. 11(c) shows the training loss function comparison for the complex model. Notably, the EfficientNetV2 network model used in this study demonstrates the smallest loss function error, outperforming the DNN and ResU-Net++ models.

Table II compares the training parameters of the three different network structures across three types of training datasets. The DNN network model's parameters are heavily influenced by the number of neurons and network layers. In contrast, both the ResU-Net++ and EfficientNetV2 models are based on the CNNs architecture, with EfficientNetV2 requiring fewer parameters than ResU-Net++.

Table III shows the training time we have calculated—our PC configuration: CPU: 1 × Intel<sup>1</sup> Xeon<sup>1</sup> Gold 5218 CPU @ 2.30 GHz; GPU: 1 × NVIDIA RTX A4000, 16 GB; and memory: 144 GB.

<sup>1</sup>Registered trademark.

TABLE III  
THREE TYPES OF NETWORK MODEL TRAINING TIME

Model Training Time	Symmetric model	Asymmetric model	Complex model
DNN	7.9min	8.4min	8.6min
ResUnet++	102.63min	113.min	108.24min
EfficientNetV2	126.72min	134.32min	119.41min

TABLE IV

HYPERPARAMETERS OF THE EFFICIENTNETV2 NETWORK ARCHITECTURE

Network Parameters	Settings
Optimizer	Adam
Learning Rate	0.001
Batch Size	64
Epoch	50
Error Function	Smooth L1 Loss

An essential aspect of training is balancing underfitting and overfitting by appropriately choosing the number of epochs. Underfitting, where the model is inadequately trained, can result from too few epochs, whereas overfitting, where the model overfits the training data, may occur with too many epochs. The specific hyperparameter settings are outlined in Table IV. Based on experimental results, we chose to train for 50 epochs, using Adam's optimizer, a learning rate of 0.001, a batch size of 64, and SmoothL1Loss as the loss function. This combination results in the EfficientNetV2 network achieving the lowest loss function error in the training dataset, compared to the other two networks.

#### B. Validating Models

To further assess the predictive capabilities of the EfficientNetV2 network, this study selects three types of basin density models from the validation dataset for verification.

1) *Symmetry Model*: Fig. 12 depicts the symmetric model, where the sedimentary basin model spans  $5000 \times 5000$  m. The density-filled element matrix has dimensions of  $200 \times 200 \times 40$  m, and the density difference between the top interface of the sedimentary basin and the surrounding rock is  $\Delta\rho_0 = -0.03$  g/cm<sup>3</sup>. Fig. 12(a) presents a slice diagram along  $X = 0$  m and  $Y = 0$  m of the basin base undulating interface and the variation in overlying strata density for the symmetric model. Here, the black line represents the actual morphology of the basin base undulating interface. Fig. 12(b) illustrates the corresponding Bouguer gravity anomaly, where the observation range extends 5000 m in both the  $X$ - and  $Y$ -directions, with a spacing of 200 m between measurement points and lines, totaling 625 observation points.

Upon inputting the Bouguer gravity anomaly data from Fig. 12(b) into the three trained network models, Fig. 13(a) shows the predicted 3-D vertical sections along  $X = 0$  m [Fig. 13(b)] and  $Y = 0$  m [Fig. 13(c)] for the basement relief interface and the overlying stratum density distribution. The blue line indicates the actual basement relief interface, the black dotted line shows the prediction by the DNNs network,

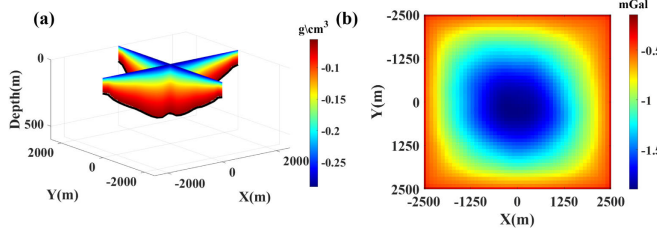


Fig. 12. Symmetrical density basement model and Bouguer gravity anomaly field. (a) Vertical sections of the 3-D model along  $X = 0$  and  $Y = 0$ , where the black line represents the true basement interface morphology. (b) Gravity anomaly forward field plot of the symmetrical density basement model.

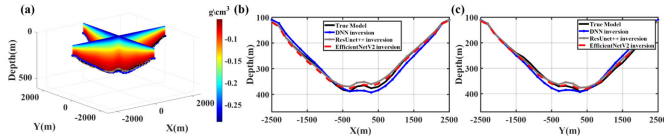


Fig. 13. Comparison of symmetric model results predicted by three networks. (a) 3-D space predicted sections along  $X = 0$  and  $Y = 0$  m. (b)  $X$ - $Z$  section of the predicted basement reliefs along  $Y = 0$  m by the three networks. (c)  $Y$ - $Z$  slice of the predicted basement reliefs along  $X = 0$  m by the three networks.

the red line shows the prediction by the ResU-Net++ network, and the yellow line shows the prediction by the EfficientNetV2 network. The DNNs' network predictions tend to be deeper than the actual model and ResU-Net++ predictions are shallower, while EfficientNetV2 closely matches the actual basin scenario.

To quantitatively evaluate the inversion results, we computed the error in the depth ( $Z$ ) and density change factor ( $\beta$ ) of the undulating interface of the basement as predicted by the three network models using (14). Fig. 14 presents the error maps of the three networks' predictions on the symmetric model. Fig. 14(a) shows the DNN network model's error in predicting the depth of the basement relief interface. Fig. 14(b) and (c) displays the error maps for the ResU-Net++ and EfficientNetV2 network models, respectively. For the density change factor predictions, Fig. 14(d)–(f) illustrates the errors for the DNN, ResU-Net++, and EfficientNetV2 models, respectively. The DNN network shows poor fitting in the upper left part of the sedimentary basin, with ResU-Net++ having significant local errors. In contrast, the EfficientNetV2 network model demonstrates relatively high accuracy in predicting the symmetric model, underscoring its superior predictive performance.

2) *Asymmetric Model*: In recognizing that real basin fluctuations are often asymmetric, our model construction process accounts for various scenarios, including the design of an asymmetric model. Fig. 15 illustrates a sedimentary basin model with dimensions of  $5000 \times 3000$  m and a density-filled unit matrix sized at  $100 \times 100 \times 40$  m. Fig. 15(a) presents a vertical slice diagram along  $X = 0$  m and  $Y = 0$  m for the asymmetric model, showcasing the uneven interface of the basin base and the density change in the overlying stratum. Fig. 15(b) depicts the Bouguer gravity anomaly for the asymmetric model, with an observation range of 6000 m along the  $X$ -direction and 4000 m along the  $Y$ -direction. The

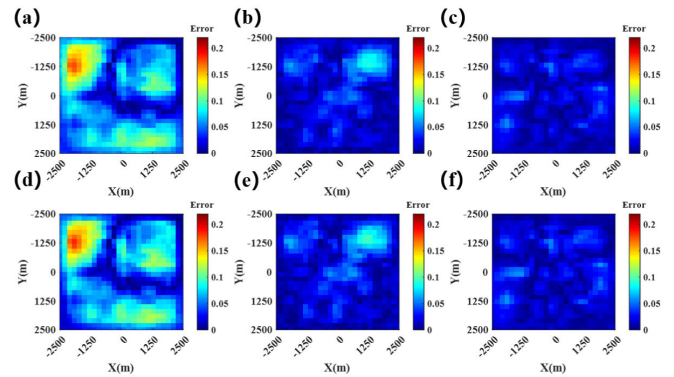


Fig. 14. Comparison of prediction results error of three network symmetric models. (a) Predicted depth error by DNN network model. (b) Predicted depth error by ResU-Net++ network model. (c) Predicted depth error by EfficientNetV2 network model. (d) Predicted density change factor  $\beta$  error by DNN network model. (e) Predicted density change factor  $\beta$  error by ResU-Net++ network model. (f) Predicted density change factor  $\beta$  error by EfficientNetV2 network model.

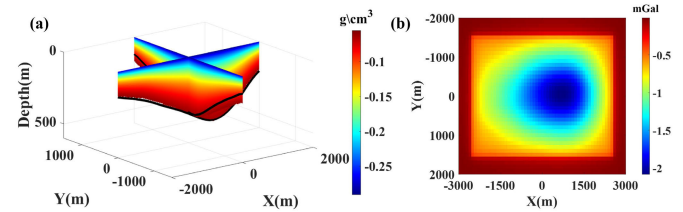


Fig. 15. Asymmetric density basement model and Bouguer gravity anomaly field. (a) Vertical sections of the 3-D model along  $X = 0$  and  $Y = 0$ , where the black line represents the true basement interface morphology. (b) Gravity anomaly forward field plot of the asymmetric density basement model.

distance between measurement points and lines is set at 100 m, totaling 2400 points.

Fig. 16, in a similar fashion, displays a comparative chart of inversion results and fitting errors. From this figure, it is evident that the predictions of the DNN network model are shallower than the true model. The ResU-Net++ network model also shows shallower predictions, while the EfficientNetV2 network model demonstrates the best fit to the model [as seen in Fig. 16(a)–(c)]. In addition, the error map reveals that the EfficientNetV2 network model yields the smallest error in both the 3-D basement relief depth [Fig. 16(d)–(f)] and the density change factor [Fig. 16(g)–(i)]. These findings affirm the effectiveness of the EfficientNetV2 model, particularly in handling asymmetric basin models where accurate representation of irregularities is crucial.

3) *Complex Model*: In actual exploration scenarios, the basement interface of a basin typically exhibits a complex structure, quite distinct from the simpler cases previously discussed. Rather than being formed from a single depression, it often consists of various depressions that appear alternately and combine to form a complex model. Echoing the methodology outlined in Sections III-B2 and III-B3, Fig. 17 illustrates a sedimentary basin model with dimensions of  $8800 \times 8800$  m and a density-filled unit matrix sized  $200 \times 200 \times 40$  m. Fig. 17(a) displays a vertical slice diagram along  $X = 0$  m and  $Y = 0$  m, showing the undulating interface of the basin base and the density change in the overlying

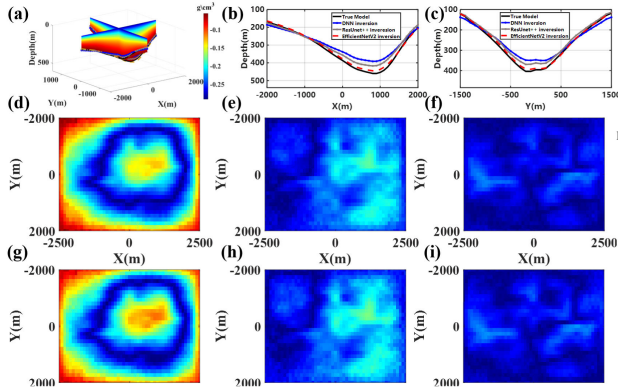


Fig. 16. Comparison of asymmetric modulus results and errors predicted by three networks. (a) 3-D prediction results. (b)  $X$ - $Z$  section of the predicted basement reliefs along  $Y = 0$  m by the three networks. (c)  $X$ - $Z$  section of the predicted basement reliefs along  $X = 0$  m by the three networks. (d) Predicted depth error by DNN network model. (e) Predicted depth error by ResU-Net++ network model. (f) Predicted depth error by EfficientNetV2 network model. (g) Predicted density change factor  $\beta$  error by DNN network model. (h) Predicted density change factor  $\beta$  error by ResU-Net++ network model. (i) Predicted density change factor  $\beta$  error by EfficientNetV2 network model.

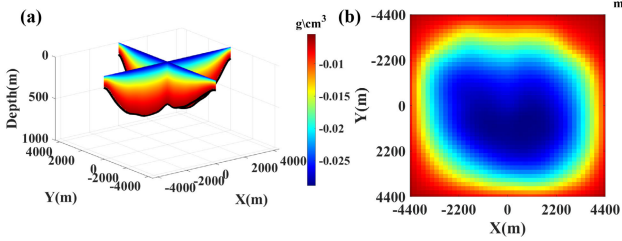


Fig. 17. Complex density basement model and Bouguer gravity anomaly field. (a) Vertical sections of the 3-D model along  $X = 0$  and  $Y = 0$ , where the black line represents the true basement morphology. (b) Gravity anomaly forward field plot of the complex density basement model.

strata for this complex model. Fig. 17(b) depicts the Bouguer gravity anomaly of the complex model, with an observation range of 4400 m along both the  $X$ - and  $Y$ -directions, a 200-m spacing between measurement points and lines, and a total of 1936 measurement points.

Fig. 18, in a similar vein, presents the prediction results and error comparisons for the complex basin model using three different network structures. The DNN network model shows the least satisfactory results, achieving only local fitting. The ResU-Net++ network model demonstrates poor fitting, especially in the upper right part of the basin. In contrast, the EfficientNetV2 network model closely approximates the real complex model.

The experimental results underscore the significant advantages of the EfficientNetV2 network model in predicting both the basement relief interface and the overlying stratum density of sedimentary basins. Its efficient structural design and effective parameter combination make it adept at accurately capturing geological features and stratigraphic variations. This leads to improved accuracy and robustness in predictions. When compared with the traditional DNN network model and the ResU-Net++ network model, the EfficientNetV2 network

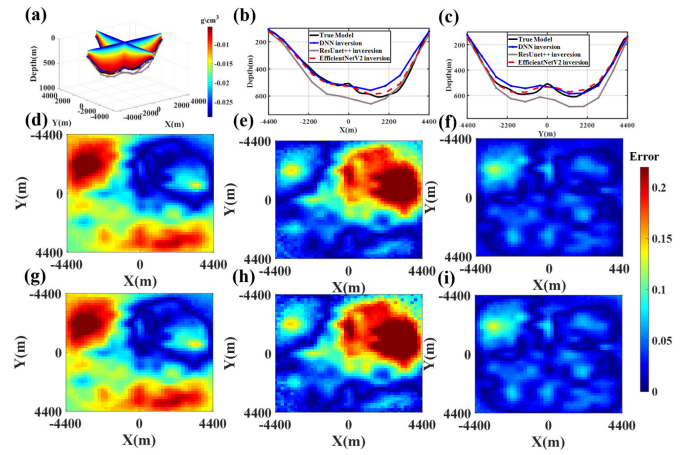


Fig. 18. Comparison of complex model results and error of three network predictions. (a) 3-D prediction results. (b)  $X$ - $Z$  section of the predicted basement reliefs along  $Y = 0$  m by the three networks. (c)  $X$ - $Z$  section of the predicted basement reliefs along  $X = 0$  m by the three networks. (d) Predicted depth error by DNN network model. (e) Predicted depth error by ResU-Net++ network model. (f) Predicted depth error by EfficientNetV2 network model. (g) Predicted density change factor  $\beta$  error by DNN network model. (h) Predicted density change factor  $\beta$  error by ResU-Net++ network model. (i) Predicted density change factor  $\beta$  error by EfficientNetV2 network model.

model not only shows a notable improvement in prediction accuracy but also excels in handling complex model structures.

4) *Robustness*: We assessed stability by adding 5% Gaussian noise to the original Bouguer gravity anomaly data and predicting results using the trained EfficientNetV2 network. Fig. 19 shows that even with noise, the deep neural network predicts results accurately, demonstrating strong robustness. This indicates that our network maintains high prediction accuracy with noisy data.

Regarding the instability and nonuniqueness issues of traditional inversion techniques, our method offers effective solutions. Traditional methods easily fall into local minima, resulting in nonunique solutions and poor performance under noise interference. However, our deep learning method enables the network to learn robust features and patterns by training with large datasets. As a result, deep neural networks provide stable and reliable prediction results even in noisy environments.

Our method also demonstrates strong noise immunity. The Gaussian noise test shows that the trained EfficientNetV2 network tolerates noise well, significantly improving the stability of traditional inversion methods under noisy conditions. This feature enhances the practicality and reliability of our method in real-world applications.

## IV. CASE STUDY

### A. Geological Background of Poyang Lake Basin

The Poyang Lake Basin, situated in northern Jiangxi Province, China, spans between  $115^{\circ}30'$  and  $117^{\circ}00'$  East longitude, and  $28^{\circ}20'$  and  $29^{\circ}30'$  North latitude, as depicted in the left panel of Fig. 20. This region, covering approximately  $11\,230$  km<sup>2</sup>, is a fault basin, formed during the Meso-Cenozoic era and laid atop Paleozoic strata. It predominantly extends

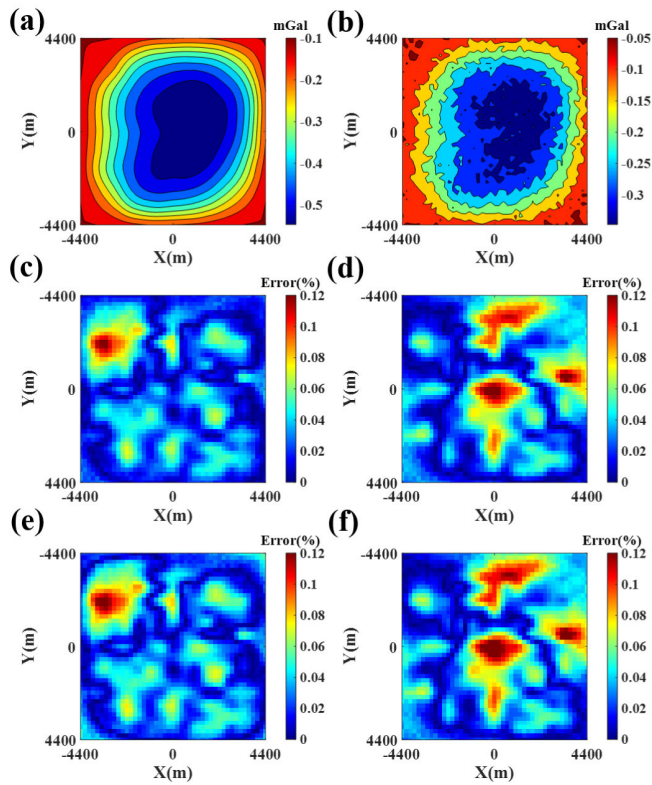


Fig. 19. Comparison of the noisy Bouguer gravity anomaly data and the EfficientNetV2 network prediction results. (a) Bouguer gravity anomaly data without noise data. (b) Bouguer gravity anomaly data with 5% Gaussian noise. (c) Basin basement depth error predicted by the EfficientNetV2 deep neural network for the noise-free data. (d) Basin basement depth error predicted by EfficientNetV2 deep neural network on 5% noise data. (e) Density change factor error predicted by EfficientNetV2 deep neural network on noiseless data. (f) Density change factor error predicted by EfficientNetV2 deep neural network on noiseless data.

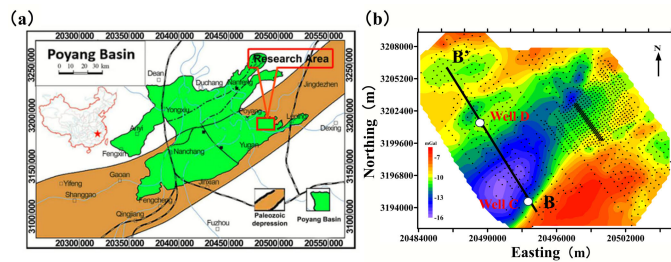


Fig. 20. Map of Poyang Lake Basin working area and Bouguer gravity anomaly. (a) Geological profile map of Poyang Lake Basin and the research work area marked with red boxes. (b) Bouguer gravity anomaly map, where the black solid line  $B-B'$  is the seismic 2-D survey line, the white solid circle is the formation verification wells (Well-C and Well-D), and the black solid points are distributed along the north-south direction of gravity observation points.

from north to east-northeast. The basin is notable for encompassing five major river systems, converging into the renowned Poyang Lake, which occupies about 3050 km<sup>2</sup> in the basin’s eastern sector.

The Upper Paleozoic tectonic landscape was primarily shaped by the NW-SE compressive stress field during the Indosinian to Early Yanshan periods. Situated south of the Changchang-Boyang line is the Nanyang Depression, with the Pingxiang-Leping Depression above it, resulting from

sea-land interactions and sedimentation from the Upper Paleozoic to the Triassic period. This region features significant thrusts and folds in the Upper Paleozoic strata, characterized by eastward and northeastward reverse faults north of the rift valley, accompanied by left-lateral strike-slip faults along northeastward trends. In the early Mesozoic era, major reverse faults transformed into tensional positive faults under the late Yanshan extension’s influence, guiding the Cretaceous sediment deposition in the depression. Thus, the Mesozoic tectonic pattern, to an extent, continues the early tectonic framework but shifts from being dominated by northeastward and northward-trending rifts to normal faults.

The Nanpoyang Depression was divided into two primary sections: west and east. The eastern section follows an NW-SE trend and includes smaller tectonic units such as the Nanjing Depression, Ruihong Uplift, and Erjiacun Depression. This study focuses on an 1120-km<sup>2</sup> area in the northeast of the Erjiacun Depression, delineated by the boundary fault and the southern edge of the Ruihong metamorphic rocks, where gravity data were collected. Dominant Mesozoic strata in this area include the Late Cretaceous Ganzhou Group and Guifeng Group. The depression’s interior hosts three Mesozoic graben-type subdepressions interspersed with uplift zones. The main fault significantly influences the depression’s tectonic morphology, with formation depths reaching about 1000 m and the deepest subdepression exceeding 3000 m. The Upper Paleozoic remnants, over 1000 m thick, represent the largest Upper Paleozoic remnant belt in the eastern part of Nanpoyang Depression. During the Indo-Chinese to Early Yanshan periods, parts of the Upper Paleozoic strata underwent folding and overturning, remaining elevated for an extended time and subject to continuous erosion. Seismic interpretations reveal substantial denudation in many Upper Paleozoic locations, while geological outcrop investigations indicate that Upper Triassic and Lower Jurassic strata are confined to specific residual tectonic syncline areas.

**B. Inversion Results and Interpretation**

To suit the EfficientNetV2 network’s requirement for a standardized matrix cell as input, the irregularly arranged Bouguer gravity anomaly data in Fig. 20(b) are interpolated to form a uniform 45 × 45 observation matrix. This matrix serves as the input for the EfficientNetV2 network. For validation purposes, the effectiveness of our approach is benchmarked against traditional smooth inversion. In addition, the seismic profile lateral line  $B-B'$  and well logs from Well-D to Well-C provide a comparative analysis of horizon densities.

1) *Training on Real Data:* In basin prediction using deep learning, it is crucial to employ training datasets that reflect the geological nuances of different work areas. While the simulation test stage’s training set showcases the advantages of the EfficientNetV2 network over the DNN and ResU-Net++ networks, these datasets may not fully capture the geological features of the target basin in actual data prediction. Thus, it is necessary to establish a dataset tailored to the geological conditions of the specific work area and adjust the parameters of the corresponding EfficientNetV2 network model to enhance prediction accuracy and reliability.

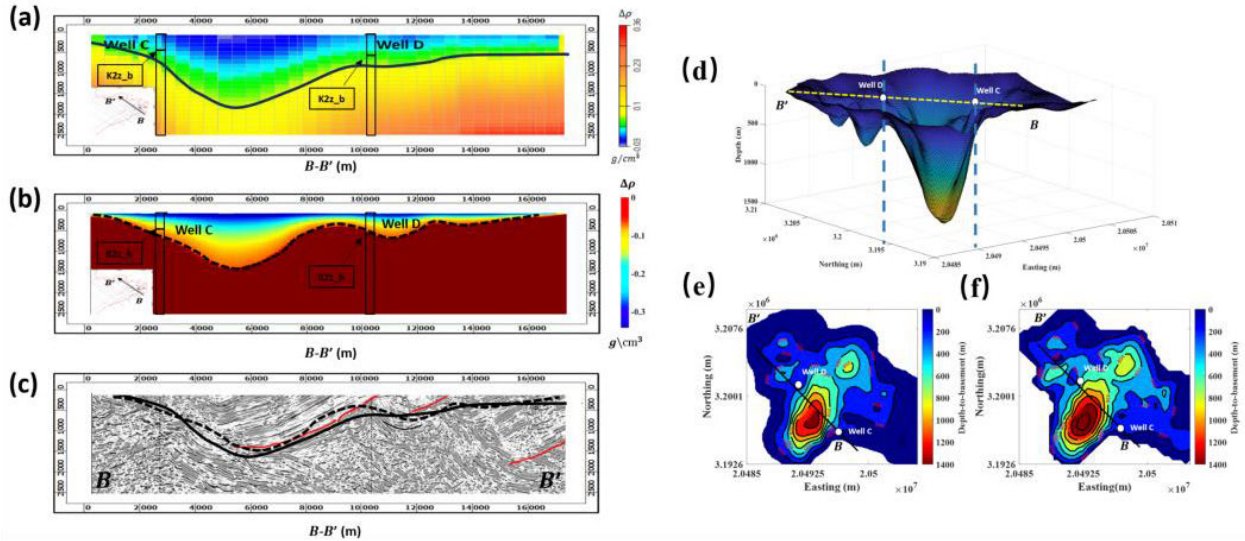


Fig. 21. Comparison of the seismic imaging along  $B-B'$  profile with different imaging results implemented by the traditional smooth and EfficientNetV2 network inversion. And 3-D-view of basement interface and the comparison of contour maps of depth-to-basement. (a) Vertical density section obtained from traditional gravity smoothing inversion. (b) Vertical density section obtained from EfficientNetV2 network. (c) Seismic imaging overlapping with traces of interfaces predicted by traditional gravity smoothing inversion and EfficientNetV2 network. (d) Schematic diagram of 3-D basement model retrieved by EfficientNetV2 network. (e) Contour map of depth-to-basement predicted by EfficientNetV2 network. (f) Contour map of depth-to-basement predicted by traditional smooth inversion results.

In this study, the actual training data label  $\{Z_{ATU}^{\psi}, \beta_{ATU}^{\psi}\}_{\psi=1}^{N_{ATU}}$ ,  $N_{ATU} = 3000$ , and corresponding training input data  $\{\Delta g_{ATU}^{\psi}\}_{\psi=1}^{N_{ATU}}$ ,  $N_{ATU} = 3000$ , derived from traditional smooth inversion based on measured Bouguer gravity anomaly data [Fig. 20(b)], are input into the EfficientNetV2 network for training. Before employing the trained EfficientNetV2 model for prediction, the irregular Bouguer gravity anomaly data in Fig. 20(b) are interpolated to create a standardized  $45 \times 45$  observation matrix for the network's input.

2) *Inversion Results and Interpretation*: Fig. 21(a) and (b) displays the vertical section plots of 3-D smooth inversion results and EfficientNetV2 inversion results along the  $B-B'$  seismic lateral line. The black lines (dashed and solid) represent the predicted sedimentary basement relief by both methods, following the peak intensity transitions in the standard jet color bar [green to yellow in Fig. 21(a) and light red to dark red in Fig. 21(b)], with a density contrast value of  $-0.08 \text{ g/cm}^3$ . Wells-C and D, projected onto all inversion sections, help verify the objective boundary. Notably, the black dashed line matches the strata markers K2z\_b, indicating the Cretaceous basement boundaries from Wells-C and D with an anomalous density range of  $-0.068$  to  $-0.097 \text{ g/cm}^3$  [61]. In contrast, the black solid line does not align with these strata markers. Projecting both black lines onto the seismic profile along  $B-B'$  [Fig. 20(c)] reveals a critical limitation of traditional inversion methods; while they generally depict the main depression effectively, they often fail to represent minor sags evident in seismic sections. This discrepancy arises from the inherent limitations in the resolution and sensitivity of traditional inversion techniques. Conversely, the EfficientNetV2-based approach proposed in our work shows significant improvement. This ML method not only captures the main depression but also distinctly identifies minor sags that traditional methods often overlook. This enhanced

capability results from the advanced feature extraction and pattern recognition abilities of the EfficientNetV2 architecture, enabling more precise and detailed inversion results.

Fig. 21(d) presents a 3-D view of the basement interface predicted by EfficientNetV2. Fig. 21(e) and (f) shows the contour maps of the depth-to-basement at 200-m intervals, constructed from the interpreted basement interfaces in Fig. 21(a) and (b). These maps, with a realistic density contrast value of  $-0.08 \text{ g/cm}^3$  within the well-measured anomalous density range of  $-0.068$  to  $0.097 \text{ g/cm}^3$ , provide a reliable reference for future seismic survey planning.

## V. CONCLUSION

Geophysical exploration plays a pivotal role in the quest for oil and gas resources, offering indispensable technical and data support. The evolution of inversion techniques presents both new opportunities and challenges in the field of geophysics. The main challenges of the traditional deterministic gravity inversion methods are related to the inherent nonuniqueness and instability of the inverse problem solutions. The Monte Carlo method requires an enormous volume of computations and is very time-consuming. Unsupervised ML methods fall short in evaluating the correlation between the model and the data, and deep learning approaches may struggle with insufficient data correlation and global information.

This article employs the EfficientNetV2 network model, which demonstrates a robust capability in mapping complex gravity field data to 3-D basin models. This is achieved through two convolutional techniques, Fused-MBConv and MBConv, combined with composite scaling techniques. In our simulation study, while DNN and ResU-Net++ networks could approximate the relief morphology of 3-D sedimentary basins and the distribution of overlying strata density, they exhibited significant discrepancies from the actual models.

Compared to EfficientNetV2, DNN and ResU-Net++ showed slower loss reduction and larger errors.

In our practical data study, we utilized both traditional smooth inversion and the EfficientNetV2 network model to predict the basement interface and overlying stratum density of the Poyang Basin. The EfficientNetV2 model's predictions for the Cretaceous basin's basal interface along the  $B-B'$  seismic line align well with the primary and secondary depressions indicated in the seismic profile. Moreover, the predicted location and anomalous density values at the Cretaceous interface in the two verification wells (Well-C and Well-D) match the depth of the Cretaceous formation (K2z\_b) and the anomalous density of laboratory rock samples from the wells.

These outcomes suggest that the EfficientNetV2 network may represent an efficient additional technique in the toolkit of gravity inversions. By retrieving the basement's undulating interface and the density changes in the overlying strata, this novel technique makes it possible to capture geological details more comprehensively, thereby enhancing the accuracy and reliability of the inversion results.

#### ACKNOWLEDGMENT

The authors would like to thank Chengdu University of Technology, Chengdu, China; the Consortium for Electromagnetic Modeling and Inversion (CEMI), University of Utah, Salt Lake City, UT, USA; and Changchun University of Science and Technology, Changchun, China.

#### REFERENCES

- [1] R. A. Willoughby, "Solutions of ill-posed problems (AN Tikhonov and VY Arsenin)," *SIAM Rev.*, vol. 21, no. 2, p. 266, 1979.
- [2] K. Ji, Y. Shen, Q. Chen, B. Li, and W. Wang, "An adaptive regularized solution to inverse ill-posed models," *IEEE Trans. Geosci. Remote Sens.*, vol. 60, 2022, Art. no. 4209715.
- [3] G. Backus and F. Gilbert, "The resolving power of gross Earth data," *Geophys. J. Int.*, vol. 16, no. 2, pp. 169–205, Oct. 1968.
- [4] G. E. Backus and J. F. Gilbert, "Numerical applications of a formalism for geophysical inverse problems," *Geophys. J. Int.*, vol. 13, nos. 1–3, pp. 247–276, Jul. 1967.
- [5] D. W. Marquardt, "An algorithm for least-squares estimation of nonlinear parameters," *J. Soc. Ind. Appl. Math.*, vol. 11, no. 2, pp. 431–441, Jun. 1963.
- [6] D. W. Marquardt, "Generalized inverses, ridge regression, biased linear estimation, and nonlinear estimation," *Technometrics*, vol. 12, no. 3, p. 591, Aug. 1970.
- [7] J. N. Franklin, "Well-posed stochastic extensions of ill-posed linear problems," *J. Math. Anal. Appl.*, vol. 31, no. 3, pp. 682–716, Sep. 1970.
- [8] M. Foster, "An application of the Wiener–Kolmogorov smoothing theory to matrix inversion," *J. Soc. Ind. Appl. Math.*, vol. 9, no. 3, pp. 387–392, Sep. 1961.
- [9] D. D. Jackson, "Interpretation of inaccurate, insufficient and inconsistent data," *Geophys. J. Int.*, vol. 28, no. 2, pp. 97–109, Jun. 1972.
- [10] A. Tarantola, *Inverse Problem Theory and Methods for Model Parameter Estimation*. Philadelphia, PA, USA: SIAM, 2005.
- [11] A. Tarantola and B. Valette, "Generalized nonlinear inverse problems solved using the least squares criterion," *Rev. Geophys.*, vol. 20, no. 2, pp. 219–232, May 1982.
- [12] M. S. Zhdanov, *Advanced Methods of Joint Inversion and Fusion of Multiphysics Data*. Singapore: Springer, 2023.
- [13] M. S. Zhdanov, *Inverse Theory and Applications in Geophysics*. Amsterdam, The Netherlands: Elsevier, 2015, p. 799.
- [14] R. Zhang, T. Li, C. Liu, X. Huang, K. Jensen, and M. Sommer, "3-D joint inversion of gravity and magnetic data using data-space and truncated Gauss–Newton methods," *IEEE Geosci. Remote Sens. Lett.*, vol. 19, pp. 1–5, 2022.
- [15] C.-C. Tseng and S.-L. Lee, "Implementation of temperature data denoising operator using steepest descent method," in *Proc. 20th Int. Symp. Commun. Inf. Technol. (ISCIT)*, Oct. 2021, pp. 150–153.
- [16] X.-H. Gao and D.-N. Huang, "Research on 3D focusing inversion of gravity gradient tensor data based on a conjugate gradient algorithm," *Chin. J. Geophys.*, vol. 60, no. 4, pp. 1571–1583, 2017.
- [17] P. Qin, D. Huang, Y. Yuan, M. Geng, and J. Liu, "Integrated gravity and gravity gradient 3D inversion using the non-linear conjugate gradient," *J. Appl. Geophys.*, vol. 126, pp. 52–73, Mar. 2016.
- [18] L. Bianco, M. Tavakoli, A. Vitale, and M. Fedi, "Multiorder sequential joint inversion of gravity data with inhomogeneous depth weighting: From near surface to basin modeling applications," *IEEE Trans. Geosci. Remote Sens.*, vol. 62, 2024, Art. no. 4700311.
- [19] T.-H. Wang, D.-N. Huang, G.-Q. Ma, Z.-H. Meng, and Y. Li, "Improved preconditioned conjugate gradient algorithm and application in 3D inversion of gravity-gradiometry data," *Appl. Geophys.*, vol. 14, no. 2, pp. 301–313, Jun. 2017.
- [20] R. Varfinezhad, M. Fedi, and M. Milano, "The role of model weighting functions in the gravity and DC resistivity inversion," *IEEE Trans. Geosci. Remote Sens.*, vol. 60, 2022, Art. no. 4507915.
- [21] Z. Chen, X. Zhang, and Z. Chen, "Combined compact and smooth inversion for gravity and gravity gradiometry data," *IEEE Trans. Geosci. Remote Sens.*, vol. 60, 2022, Art. no. 5903210.
- [22] N. Wang, G. Ma, L. Li, T. Wang, and D. Li, "A density-weighted and cross-gradient constrained joint inversion method of gravity and vertical gravity gradient data in spherical coordinates and its application to lunar data," *IEEE Trans. Geosci. Remote Sens.*, vol. 60, 2022, Art. no. 4511211.
- [23] B. Chen, S. Li, Y. Sun, J. Du, J. Liu, and G. Qi, "Joint inversion of gravity gradient tensor data based on  $L_1$  and  $L_2$  norms," *IEEE Trans. Geosci. Remote Sens.*, vol. 60, 2022, Art. no. 5925208.
- [24] Z. Li and C. Yao, "An investigation of  $L_p$ -norm minimization for the artifact-free inversion of gravity data," *Remote Sens.*, vol. 15, no. 14, p. 3465, Jul. 2023.
- [25] X. Feng, W. Wang, and B. Yuan, "3D gravity inversion of basement relief for a rift basin based on combined multinorm and normalized vertical derivative of the total horizontal derivative techniques," *Geophysics*, vol. 83, no. 5, pp. G107–G118, Sep. 2018.
- [26] X. Feng, S. Liu, R. Guo, P. Wang, and J. Zhang, "Gravity inversion of blocky basement relief using  $L_0$  norm constraint with exponential density contrast variation," *Pure Appl. Geophys.*, vol. 177, no. 8, pp. 3913–3927, Aug. 2020.
- [27] F. Press, "Earth models consistent with geophysical data," *Phys. Earth Planet. Interiors*, vol. 3, pp. 3–22, Jan. 1970.
- [28] F. Press, "Earth models obtained by Monte Carlo inversion," *J. Geophys. Res.*, vol. 73, no. 16, pp. 5223–5234, Aug. 1968.
- [29] F. Press, "Regionalized Earth models," *J. Geophys. Res.*, vol. 75, no. 32, pp. 6575–6581, Nov. 1970.
- [30] M. Sambridge and K. Mosegaard, "Monte Carlo methods in geophysical inverse problems," *Rev. Geophys.*, vol. 40, no. 3, pp. 3–1–3–29, Sep. 2002.
- [31] V. I. Keilis-Borok and T. B. Yanovskaja, "Inverse problems of seismology (structural review)," *Geophys. J. Int.*, vol. 13, nos. 1–3, pp. 223–234, Jul. 1967.
- [32] L. Li and G. Ma, "The inversion of seabed terrain of the South China Sea by simulated annealing based on gravity gradient data," *Prog. Geophys.*, vol. 29, no. 2, pp. 931–935, Aug. 2014.
- [33] X. Ke, Y. Wang, and H. Xu, "3D density inversion with genetic algorithm," *J. Geodesy Geodynamics*, vol. 29, no. 1, pp. 41–45, Jan. 2009.
- [34] V. Chakravarthi, S. R. Sastry, and B. Ramamma, "MODTOHAFSD—A GUI based Java code for gravity analysis of strike limited sedimentary basins by means of growing bodies with exponential density contrast–depth variation: A space domain approach," *Comput. Geosci.*, vol. 56, pp. 131–141, Jul. 2013.
- [35] L. F. Athy, "Density, porosity, and compaction of sedimentary rocks," *AAPG Bull.*, vol. 14, no. 1, pp. 1–24, 1930.
- [36] L. Cordell, "Gravity analysis using an exponential density–depth function; San Jacinto Graben, California," *Geophysics*, vol. 38, no. 4, pp. 684–690, Aug. 1973.
- [37] H. Granser, "Three-dimensional interpretation of gravity data from sedimentary basins using an exponential density–depth function," *Geophys. Prospecting*, vol. 35, no. 9, pp. 1030–1041, Nov. 1987.
- [38] Y. Chai and W. J. Hinze, "Gravity inversion of an interface above which the density contrast varies exponentially with depth," *Geophysics*, vol. 53, no. 6, pp. 837–845, Jun. 1988.

- [39] V. Chakravarthi, M. P. Kumar, B. Ramamma, and S. R. Sastry, "Automatic gravity modeling of sedimentary basins by means of polygonal source geometry and exponential density contrast variation: Two space domain based algorithms," *J. Appl. Geophys.*, vol. 124, pp. 54–61, Jan. 2016.
- [40] H. Cai and M. Zhdanov, "Application of cauchy-type integrals in developing effective methods for depth-to-basement inversion of gravity and gravity gradiometry data," *Geophysics*, vol. 80, no. 2, pp. G81–G94, Mar. 2015.
- [41] M. H. P. Bott, "The use of rapid digital computing methods for direct gravity interpretation of sedimentary basins," *Geophys. J. Int.*, vol. 3, no. 1, pp. 63–67, Mar. 1960.
- [42] D. W. Oldenburg, "The inversion and interpretation of gravity anomalies," *Geophysics*, vol. 39, no. 4, pp. 526–536, 1974.
- [43] R. L. Parker and S. P. Huestis, "The inversion of magnetic anomalies in the presence of topography," *J. Geophys. Res.*, vol. 79, no. 11, pp. 1587–1593, Apr. 1974.
- [44] S. Liu and S. Jin, "3-D gravity anomaly inversion based on improved guided fuzzy C-means clustering algorithm," *Pure Appl. Geophys.*, vol. 177, no. 2, pp. 1005–1027, Feb. 2020.
- [45] J. Marques-Silva, T. Gerspacher, M. C. Cooper, A. Ignatiev, and N. Narodytka, "Explaining Naive Bayes and other linear classifiers with polynomial time and delay," in *Proc. Adv. Neural Inf. Process. Syst.*, vol. 33, 2020, pp. 20590–20600.
- [46] M. Li, Y. Li, N. Wu, Y. Tian, and T. Wang, "Desert seismic random noise reduction framework based on improved PSO-SVM," *Acta Geodaetica et Geophysica*, vol. 55, no. 1, pp. 101–117, Mar. 2020.
- [47] A. Özbeyaz and M. Söylemez, "Modeling compaction parameters using support vector and decision tree regression algorithms," *TURKISH J. Electr. Eng. Comput. Sci.*, vol. 28, no. 5, pp. 3079–3093, Sep. 2020.
- [48] C. J. Leggetter and P. C. Woodland, "Maximum likelihood linear regression for speaker adaptation of continuous density hidden Markov models," *Comput. Speech Lang.*, vol. 9, no. 2, pp. 171–185, Apr. 1995.
- [49] P. S. Paul, "Predictors of work injury in underground mines—An application of a logistic regression model," *Mining Sci. Technol. (China)*, vol. 19, no. 3, pp. 282–289, May 2009.
- [50] D. Ruppert, "Empirical-bias bandwidths for local polynomial nonparametric regression and density estimation," *J. Amer. Stat. Assoc.*, vol. 92, no. 439, p. 1049, Sep. 1997.
- [51] S. He, H. Cai, S. Liu, J. Xie, and X. Hu, "Recovering 3D basement relief using gravity data through convolutional neural networks," *J. Geophys. Res., Solid Earth*, vol. 126, no. 10, Oct. 2021, Art. no. e2021JB022611.
- [52] S. Zhao, D. Liu, Q. Yuan, and J. Li, "A global gravity reconstruction method for mercury employing deep convolutional neural network," *Remote Sens.*, vol. 12, no. 14, p. 2293, Jul. 2020.
- [53] R. F. Annan and X. Wan, "Recovering bathymetry of the Gulf of Guinea using altimetry-derived gravity field products combined via convolutional neural network," *Surveys Geophys.*, vol. 43, no. 5, pp. 1541–1561, Jul. 2022.
- [54] D. Jha et al., "ResUNet++: An advanced architecture for medical image segmentation," in *Proc. IEEE Int. Symp. Multimedia (ISM)*, Dec. 2019, pp. 2250–2255.
- [55] O. Ronneberger, P. Fischer, and T. Brox, "U-Net: Convolutional networks for biomedical image segmentation," in *Medical Image Computing and Computer-Assisted Intervention—MICCAI*. Cham, Switzerland: Springer, 2015, pp. 234–241.
- [56] H. Chen et al., "A landslide extraction method of channel attention mechanism U-Net network based on Sentinel-2A remote sensing images," *Int. J. Digit. Earth*, vol. 16, no. 1, pp. 552–577, Oct. 2023.
- [57] X. Zhou, Z. Chen, Y. Lv, and S. Wang, "3-D gravity intelligent inversion by U-Net network with data augmentation," *IEEE Trans. Geosci. Remote Sens.*, vol. 61, 2023, Art. no. 5902713.
- [58] M. Tan and Q. Le, "EfficientNet: Rethinking model scaling for convolutional neural networks," in *Proc. 36th Int. Conf. Mach. Learn.*, 2019, pp. 6105–6114.
- [59] M. Tan and Q. Le, "EfficientNetV2: Smaller models and faster training," in *Proc. 38th Int. Conf. Mach. Learn.*, 2021, pp. 10096–10106.
- [60] V. A. Litinsky, "Concept of effective density; Key to gravity depth determinations for sedimentary basins," *Geophysics*, vol. 54, no. 11, pp. 1474–1482, 1989.
- [61] Z. Xu, R. Wang, W. Xiong, J. Wang, and D. Wang, "3D hybrid imaging based on gravity migration and regularized focusing inversion to predict the Poyang basin interface," *Geophysics*, vol. 86, no. 4, pp. G55–G67, Jul. 2021.



**Yu Zhang** received the B.S. degree in geophysics from Chengdu University of Technology, Chengdu, China, in 2023, where he is currently pursuing the Ph.D. degree.

His research interests include gravity and magnetic inversion imaging.



**Zhengwei Xu** received the M.Sc. degree in geo-exploration science and information technology from Jilin University, Changchun, China, in 2008, and the Ph.D. degree in geophysics from the University of Utah, Salt Lake City, UT, USA, in 2013.

He is currently a Researcher with the College of Geophysics, Chengdu University of Technology, Chengdu, China. His research interests include gravity, magnetic, and electromagnetic forward modeling and inversion theory, as well as incorporation and joint inversion of multigeophysical data using artificial intelligence.



**Minghao Xian** received the B.S. degree in geophysics from Chengdu University of Technology, Chengdu, China, in 2023, where he is currently pursuing the M.S. degree.

His research interests include gravity and magnetic inversion imaging.



**Michael S. Zhdanov** (Senior Member, IEEE) received the M.Sc. degree in geophysics from Moscow Gubkin State University of Oil and Gas, Moscow, Russia, in 1968, and the Ph.D. degree in physics and mathematics from Moscow State University, Moscow, in 1970.

He was the Founding Director of the Geoelectromagnetic Research Institute, Russian Academy of Sciences, Moscow, and the Deputy Director of the Institute of Terrestrial Magnetism, Ionosphere and Radio Wave Propagation, Russian Academy of

Sciences. He is currently a Distinguished Professor with the Department of Geology and Geophysics, University of Utah, Salt Lake City, UT, USA; the Director of the Consortium for Electromagnetic Modeling and Inversion (CEMI), University of Utah; and the CEO and the Chairperson of TechnoImaging, Salt Lake City. He is also an Honorary Gauss Professor with Göttingen Academy of Sciences, Göttingen, Germany, and an Honorary Professor with China National Centre for Geological Exploration Technology, Beijing, China. His research interests include fundamental and applied geophysics, inversion theory, electromagnetic theory and methods, as well as integration and joint inversion of multiphysics data.

Dr. Zhdanov is a fellow of the Russian Academy of Natural Sciences, the Electromagnetics Academy, USA, and an Honorary Member of the Society of Exploration Geophysicists.



**Changjie Lai** received the B.S. degree in geophysics from Xi'an Shiyou University, Xi'an, China, in 2010, and the M.Sc. degree from China University of Petroleum, Beijing, China, in 2013.

His research interests include basic geological survey and resource evaluation of unconventional oil and gas.



**Lifeng Mao** received the M.Sc. and Ph.D. degrees in geophysics from Chengdu University of Technology (CDUT), Chengdu, China, in 2004 and 2007, respectively.

He is currently a Professor with the College of Geophysics, CDUT. His research interests include the forward and inversion theory of geophysical electromagnetic methods, with a focus on the 3-D simulation of electromagnetic fields in both time and frequency domains.



**Rui Wang** received the Ph.D. degree in traffic and transportation engineering from Jilin University, Changchun, China, in 2014.

He is currently an Associate Professor and the Head of the Software Engineering Department, School of Computer Science and Technology, Changchun University of Science and Technology, Changchun. His main research interests include machine learning, computer vision, and geophysics.



**Guangdong Zhao** received the B.S. degree in prospecting technology and engineering from Chang'an University, Xi'an, China, in 2015, and the Ph.D. degree in geophysical prospecting and information technology from Central South University, Changsha, China, in 2021.

He is currently an Associate Researcher with the College of Geophysics, Chengdu University of Technology, Chengdu, China. His research interests include forward and inversion modeling methods of gravity and magnetic, with the application to lunar mascon basins and the Tibetan plateau.